IEEE Access
Multidisciplinary | Rapid Review | Open Access Journal

Received 2 September 2024, accepted 16 September 2024, date of publication 27 September 2024,
date of current version 25 October 2024.

Digital Object Identifier 10.1109/ACCESS.2024.3469540

RESEARCH ARTICLE

Enhanced Multiphase Interleaved Boost Converter Interface for Grid-Connected PV Power System

RASHA KASSEM[1], NAGWA F. IBRAHIM[2], MOHAMED METWALLY MAHMOUD[3], ABDULAZIZ ALKUHAYLI[4], (Member, IEEE), USAMA KHALED[2], ABDERRAHMANE BEROUAL[5], (Life Fellow, IEEE), AND HEDRA MAHFOUZ IBRAHIM SALEEB[1]

[1]Electrical Department, Faculty of Technology and Education, Sohag University, Sohag 82524, Egypt
[2]Electrical Department, Faculty of Technology and Education, Suez University, Suez 43533, Egypt
[3]Electrical Engineering Department, Faculty of Energy Engineering, Aswan University, Aswan 81528, Egypt
[4]Electrical Engineering Department, College of Engineering, King Saud University, Riyadh 11421, Saudi Arabia
[5]AMPERE Laboratory, CNRS UMR 5005, Ecole Centrale de Lyon, University of Lyon, 69130 Ecully, France

Corresponding authors: Hedra Mahfouz Ibrahim Saleeb (Hedra_Mahfouz@techedu.sohag.edu.eg) and Mohamed Metwally Mahmoud (Metwally_m@aswu.edu.eg)

This work was supported by the Researchers Supporting Project, King Saud University, Riyadh, Saudi Arabia, under Grant RSP2024R258.

ABSTRACT This paper presents a new soft switching (SS) multiphase interleaved boost converter (MIBC) consisting of three boost converters (BCs) that operate rapidly and efficiently to charge a lithium-ion battery for photovoltaic (PV) power system applications. This suggested converter can operate both active power switches at zero current switching (ZCS), and when switched off, it works at zero voltage switching (ZVS), which reduces switching losses and increases switching efficiency (SF). An interleaving structure is employed to decrease the conduction losses and reduce the input current ripple (ICR) and output voltage ripple (OVR) to increase the power rating. The suggested converter regulates the input and output power by modulating the phase shift in the pulse width modulation (PWM) technique using the maximum power point tracking (MPPT) algorithm via two closed feedback loops, one for a slower external loop and the other for a faster PWM control internal loop, similar to current mode control. The suggested converter has high voltage (HV) gain due to the coupled inductors (CIs), which act as a transformer. This magnetic design structure in both the steady-state and transient states also decreases the size and enhances the converter's performance. Finally, the suggested converter was experimentally verified on a 285W prototype, and the maximum efficiency was found to be 98%, based on modeling and experimental data.

INDEX TERMS Coupled inductor, interleaved boost converter, MPPT, photovoltaic, soft-switching, zero current switching.

ABBREVIATIONS

List of abbreviations used in this manuscript:

ARC	Auxiliary Resonant Circuit
AS	Auxiliary Switch
BCs	Boost Converters
CIs	Coupled Inductors
CS	Current Stress
DC	Duty Cycle
EMI	Electro Magnetic Interference
FCs	Fuel Cells
HS	Hard Switching
HV	High Voltage
ICR	Input Current Ripple
LV	Low Voltage
MIBC	Multiphase Interleaved Boost Converter
MPPT	Maximum Power Point Tracking

The associate editor coordinating the review of this manuscript and approving it for publication was Inam Nutkani.

© 2024 The Authors. This work is licensed under a Creative Commons Attribution-NonCommercial-NoDerivatives 4.0 License.
For more information, see https://creativecommons.org/licenses/by-nc-nd/4.0/

MS	Main Switch
OF	Output Filter
OVR	Output Voltage Ripple
P&O	Perturb & Observe
PFC	Power Factor Correction
PIC	Programmable Interface Controllers
PV	Photo Voltaic
PWM	Pulse Width Modulation
RCs	Resonant Capacitors
RES	Renewable Energy sources
RF	Resonance Frequency
RIs	Resonant Inductors
RMS	Root Mean Square
SF	Switching Frequency
SS	Soft Switching
WTs	Wind Turbines
ZCS	Zero Current Switching
ZVS	Zero Voltage Switching

I. INTRODUCTION

In the last few decades, the use and depletion of fossil fuels have accelerated in parallel with the significant increase in electricity demand [1], [2]. Solar energy (PV) is one of the most commonly used renewable energy sources (RESs), and it is a clean and noiseless energy source that does not emit greenhouse gases [3], [4]. RES has emerged as a new generation method, with multiple converter topologies and control strategies [5], additionally; it has less maintenance and moderate efficiency [6]. In 2018, at least 1GW of generating capacity had been installed in more than 90 countries, while more than 30 countries reached a 10 GW capacity. In some areas, wind turbines (WTs) and PV power have further expanded their percentages and an increasing number of countries now have variable renewables in the energy mixes of more than 20% [7], [8]. According to the International Energy Agency [9], and the United Nations Environment Programme [10], PV energy generation is experiencing consistent growth day by day, motivated by the concerns of climate change, high oil prices, and incentives for renewable energy usage.

The DC power generated by the PV array is limited and depends on sunshine, which varies over different periods of the day as well as different seasons. Weather conditions are one of the main problems in installing PV panels, so the solution to this problem is to use maximum power point tracking (MPPT) in the PV power system [11], [12]. MPPT can ensure that the PV can obtain MP under irradiation conditions and temperature changes over time. MPPT represents the MP in the PV system by changing the voltage and current at the load [13]. PV panels can obtain MP by using conventional algorithms such as perturb and observe (P&O) [14]. The P&O algorithm can track the MPP when the irradiation state and temperature fluctuate [12]. The application of the P&O algorithm for PV energy harvesting chips was reported in [15]. From the results, it was found that the P&O method could track a better energy of the PV [16]. The P&O applications were also reported in [17].

However, this algorithm has the disadvantage that it has a large output power ripple when operating under normal conditions. This is because the P&O algorithm uses a fixed perturbation step size, so it cannot have a fast response performance and high accuracy simultaneously [18]. If the step size is set too small, the response speed will be slow to track the MPP when temperature and irradiation conditions change [19]. Meanwhile, the response will have a large enough ripple at a steady state when the step size is set too large [20]. The efficiency of a PV system depends not only on the MPPT algorithm used but also on the type of DC-DC converter topologies adopted in the system [21]. It has been reported that system performance was limited by the type of converter used [22]. The main requirement of any converter used in the MPPT system is that it should have a low input current ripple and follow-up of the full range of impedance of the PV source [23]. That boost or its derived topologies present a low current ripple on the PV side, but a high ripple on the load side [24]. Another issue that has been encountered is the low efficiency of the converters and the high cost of designing a converter that can boost and smooth the output voltage to suit the power system requirement [25]. High-efficiency BCs are essential for RES interface circuits [26], as shown in Fig. 1. Most RES, such as WTs, fuel cells (FCs), and PV, have low and unregulated output voltages [27]. Furthermore, the designed DC-DC converter boosting applicability and compatibility will be tested. Many proposed topologies have been proposed to boost voltage with higher efficiency; among the important studies are the following: the works presented in [28] and [29]. A battery or an inverter is often the load for this interface circuit, which must generate a DC-HV from a low voltage (LV) [30]. High-frequency BCs are widely used in charging batteries from RES due to their considerable advantages of higher power density, quick response, and ease of control [31]. It is also utilized in power factor correction (PFC) circuits [32]. The SF of boost converters increases to lower their size and weight [33]. When these traditional IBCs, as shown in Fig. 2, are powered by high-frequency switching, they cause an increase in current stress (CS) in the switches [34], resulting in more power losses and lower circuit efficiency [35]. Several soft-switching techniques such as zero-voltage-switching (ZVS) and zero-current-switching (ZCS) were proposed to reduce the input current ripple [36]. However, these options often require additional components such as auxiliary switches, smoothing inductors, and clamp capacitors, resulting in high unit cost, increased ohmic losses, and reduced converter efficiency, thereby hampering the efficiency used in [37]. overall system performance [38]. The SS techniques like ZCS or ZVS decrease the switching losses.

This approach is used in the suggested converter, as indicated in Fig. 3. Increasing the number of phases improves efficiency, but the converter control design becomes

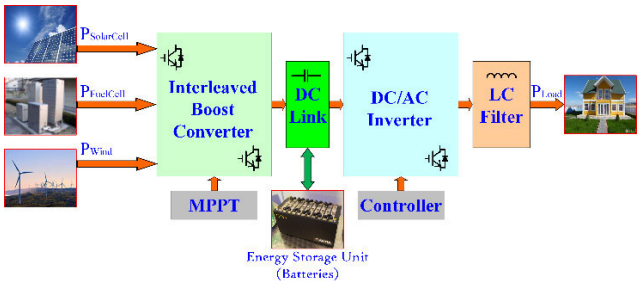

FIGURE 1. Schematic diagram of the RES interface circuit.

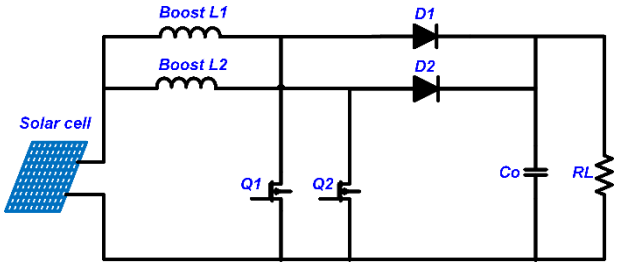

FIGURE 2. Traditional hard switching (HS) of IBC.

complex [39]. The interleaving structure is employed to raise the power rating, as it consists of CIs connected in parallel [40], as seen in Figure 3. The current path is split into three parts hence the ICR can be decreased, switching losses reduced, and increased efficiency [41]. ZCS-BCs technology is appropriate when using MOSFET switches to lower both conduction and capacitive operational losses [42]. In addition; it reduces passive components and electromagnetic interference (EMI) [43]. The several ZCS-BCs are presented in [44]. The two more switches are employed to create SS circumstances [45]. However, the interleaving structure is used in [46]. The peak current for semiconductor switches in the converter is high [47]. Furthermore, the di/dt is greater than the suggested MIBC resulting in increased switching losses and EMI harmonics [48]. The main switches (MS) are activated in the ZCS state but are deactivated in the HS state [49].

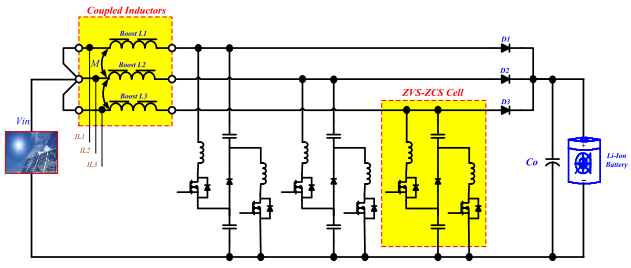

FIGURE 3. The suggested 3-phase IBC configuration.

MIHC is considered an emerging topology for DC-DC converters, due to its boosting capability. The main and novelty contributions to this work are summarized as follows:

- Achieve high efficiency by reducing ripple currents with an interleaving structure and conserving energy.
- The suggested converter can step up the low-level input DC voltage into a high-level output DC voltage and utilize a minimum number of power switches.
- A double-loop control approach is used to achieve the quick transient response, where one loop limits the inductor current and the other limits the ripple in the output voltage.
- The converter control system independently charges/discharges the battery using several current regulator loops for input DC sources and voltage regulator loops to balance the power flow.

The remainder of the paper is organized as follows: This paper provides an overview of soft switching, specifically an auxiliary resonant circuit suggested in Section I. The operating precept and steady-state study of the suggested MIBC are explained in Section II. Optimal design ideas for circuit parameters of the suggested MIBC are presented in Section III. Evaluation of efficiency and converter losses is performed in Sections IV and V, respectively. The simulation results of the suggested MIBC and experimental results are presented in Section VI of this paper. Concluding remarks are provided in Section VII.

II. THE SUGGESTED MULTIPHASE INTERLEAVED BOOST CONVERTER

A. CIRCUIT DESCRIPTION

Several phases of the suggested BC can be connected in parallel to form the circuit of the suggested SS-MIBC, as shown in Fig. 3. Each converter is surrounded by a phase difference of 2π/N radians, where N is the number of phases of the suggested converter. Since the suggested converter consists of 3 ph., the converters have a phase difference of 120 degrees, making all phases of MIBC operation symmetrical. Fig. 4 shows the circuit design of the suggested SS one-phase MIBC, which uses an auxiliary resonant circuit. The one-phase MIBC circuit proposed in Figure 4 consists of two MOSFET switches, i.e., a MS Q1, and an auxiliary switch (AS) Q2. The ARC consists of two resonant inductors (RIs) (Lr1 and Lr2) connected in series with the MS and AS, and two resonant capacitors (RCs) (Cr1 and Cr2) connected in parallel with the inductors and switches, as shown in Fig. 4. The OF capacitor Co with the load and resistance Ro are connected in parallel to smooth out of OVR.

This proposed converter can operate both the MS Q1 and the AS Q2 together at the beginning of the operating period, to achieve a ZCS, and operate together again at the end of the operating period, to achieve a ZVS, which reduces switching losses and increases switching efficiency. Unlike other converters mentioned in the literature review, the AS Q2 works throughout the operating period with the MS Q1, which leads to increased losses in the circuit and reduced efficiency. The suggested MIBC operates in two stages [50]. The first period is when the MOSFET is turned on, where an electric current passes from the source to the inductor

then passes through the MOSFET and returns to the source. During this period, the inductor stores part of the current passing through it. The second stage is when the MOSFET is turned off, and the inductor discharges the current stored in the load. We note that the voltage on the load terminals is the aggregate of the inductor and source voltage.

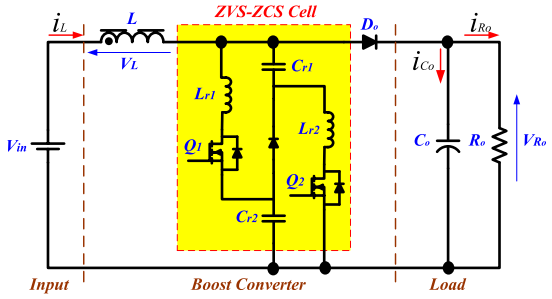

FIGURE 4. One-phase MIBC circuit.

B. OPERATION MODES AND ANALYSIS OF THE SUGGESTED CONVERTER

Figure 4 illustrates the circuit design of the suggested MIBC. The suggested layout is comparable to a traditional boost converter except for the auxiliary resonant circuit and CIs. The steady-state operating modes of the suggested MIBC in discontinuous conduction mode (DCM) are explained in detail. Figure 5 illustrates the main operational waves of the suggested MIBC in the steady state. Each switching cycle is split into four operation modes. The operation circuits are shown in Figure 6, to explain the operating intervals of the suggested MIBC.

Interval 1: (t0 ≤ t ≤ t1): It starts when both the MS Q1 and the AS Q2 are turned on together at t0 as shown in Figures 5 and equivalent circuit 6(a). In this interval, the stabilization diodes (QD1 and QD2) are turned off. Then, the current passing through the boost CIs iL and the switches currents (iLr1 and iLr2) gradually increase from the initial value of zero with the resulting resonant using (Lr and Cr). Therefore, both switches (Q1 and Q2) can be turned on at ZVS operating mode. Through this period, the current iL can be expressed following [51]:

$$I_L = i_{Lr1}(t) = i_{Lr2}(t) = (V_{in} + V_o)\sqrt{\frac{C_r}{L_r}}sin\omega_r(t) \qquad (1)$$

where $\omega_r = \frac{1}{\sqrt{L_r C_r}}$ is the angular resonance frequency (RF).

Interval 2: ($t_1 \leq t \leq t_2$): It starts when the MS Q_1 is turned on and the AS Q_2 is turned off at t_1 as shown in Figures 5 and equivalent circuit 6(b). In this interval, the energy stored in the RI L_{r2} is transmitted to the output load by the stabilizing diode Q_{D2}, because the AS Q_2 is turned off. When the inductance current iL_2 drops linearly until it reaches zero at $t = t_2$, the stabilizing diode Q_{D2} is turned off. The voltage across the AS Q_2 gradually increases from zero due to the presence of the RC C_{r2}. Therefore, the MS Q_1 is turned on at the ZCS operating mode, while the AS Q_2 is turned on at the ZVS operating mode. The current flow in the RI iL_{r2} at time $t = t_2$ can be obtained following:

$$I_{Lr2} = i_{Lr}(t_2) = \frac{\sqrt{V_o(2V_{in} + V_o)}}{Z_r} \qquad (2)$$

$$t_2 = \frac{1}{\omega_r} cos^{-1}\frac{V_{in}}{V_{in} + V_o} \qquad (3)$$

Interval 3: ($t_2 \leq t \leq t_3$): It starts when both the MS Q_1 and the AS Q_2 are turned on together at t_2 as shown in Figures 5 and equivalent circuit 6(c). In this interval, the stabilization diodes (Q_{D1} and Q_{D2}) are turned off. Then, the current passing through the boost CIs iL and the switches currents (iL_{r1} and iL_{r2}) gradually increase from the initial value of zero with the resulting resonant using (L_r and C_r). Therefore, both switches (Q_1 and Q_2) can be turned on at ZVS operating mode.

Interval 4: ($t_3 \leq t \leq t_4$): It starts when the MS Q_1 is turned off and the AS Q_2 is turned on at t_3 as shown in Figures 5 and equivalent circuit 6(d). In this interval, the energy stored in the RI L_{r1} is transmitted to the output load by the stabilizing diode Q_{D1}, because the MS Q_1 is turned off. When the inductance current iL_1 drops linearly until it reaches zero at $t = t_4$, the stabilizing diode Q_{D1} is turned off. The voltage across the MS Q_1 gradually increases from zero due to the presence of the RC C_{r1}. Therefore, the MS Q_1 is turned on at the ZVS operating mode, while the AS Q_2 is turned on at the ZCS operating mode. The current flow in the RI iL_{r1} at time $t = t_4$ can be obtained following:

$$I_{Lr1} = i_{Lr}(t_4) = \frac{V_{in}}{L_r}(DT - t_4) + I_{Lr2} \qquad (4)$$

where $D = \frac{T_{on}}{T}$ is the duty cycle (DC) of (Q_1 and Q_2).

The steady-state operating modes of the suggested MIBC are explained in detail. As a result, the suggested MIBC is only advantageous in terms of efficiency and component strain when DC is greater than 0.5. Therefore, the suggested MIBC is recommended for applications where DC is greater than 0.5.

C. MPPT CONTROLLER DESIGN FOR MIBC

The MPPT technique utilized in this paper is the perturb & observe (P&O) method. This method is based on the variation in PV power caused by a variation in voltage [50], [52]. The value of the PV input voltage VPV and the PV input current IPV are sensed and from this, the output power of the PV array can be calculated as shown in Figure 7. MPPT technique utilized these two values to control the max power, as shown in Eq. (5).

$$V_{MPP} = K_1\left(\frac{dP_{PV}}{dV_{PV}}\right)dt \qquad (5)$$

A comparison is made between the value of the calculated power and the voltage for the Kth instant and K -1th instant. If the measured voltage rating is greater than the previous value, the mean power difference (ΔP) is positive, increase

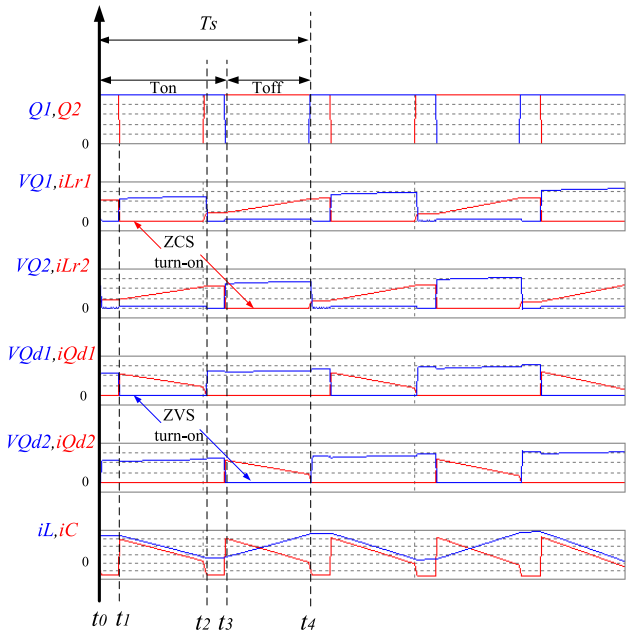

FIGURE 5. Relevant voltage and current waves of suggested MIBC.

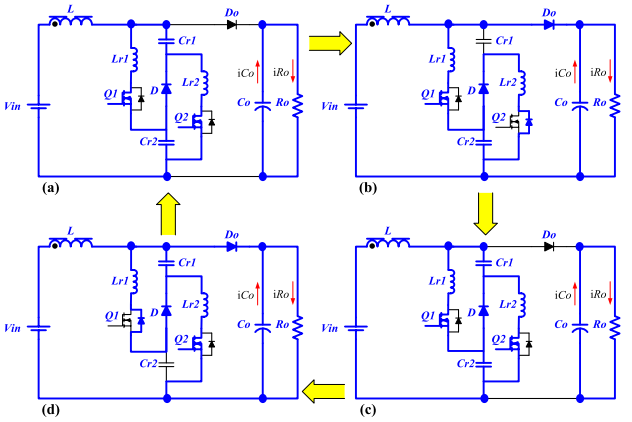

FIGURE 6. The equivalent circuits for suggested MIBC operating modes.

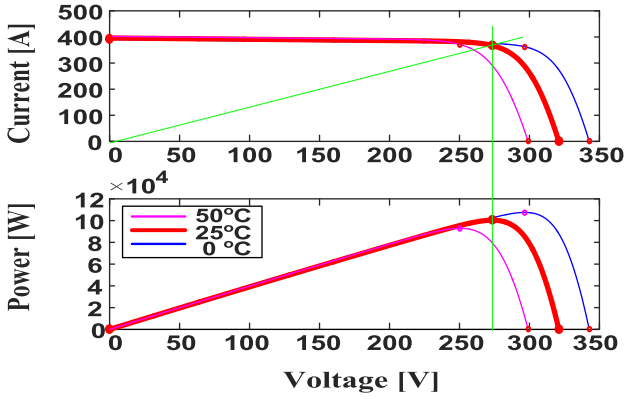

FIGURE 7. The I-V and P-V characteristic curves at various PV module temperatures at a constant solar radiation level.

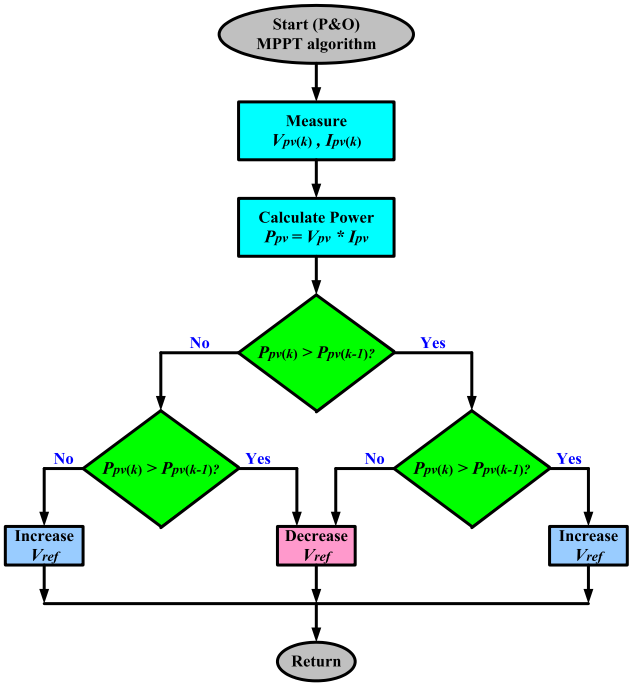

FIGURE 8. The P&O MPPT flowchart for MIBC.

the voltage reference value provided that the voltage comparator is negative, and reduce the voltage reference value if the voltage comparison is positive. If the measured voltage rating is less than the previous value, the mean power difference (P) is negative, increase the voltage reference value provided that the voltage comparison is positive, and reduce the voltage reference value if the voltage comparison is negative as shown in Figure 8 a flowchart of the implementation steps for the P&O technology.

Finally, a PWM signal is produced to turn on the switches (Q1 and Q2) in the block diagram given in Figure 9.

D. CLOSED-LOOP CONTROLLER DESIGN FOR MIBC

The DC bus is intended to be regulated by the PI controller. The MIHC control is based on two basic loops, the inner and outer loop, as seen in Fig. 9. The inner loop is thought of as current control, and the outer loop is voltage control. Fig. 10 illustrates how to obtain a closed-loop control method for the MIHC.

where the feedback transfer function is H(s), the process transfer function is Gpwm(s), and the PI controller transfer function is C(s), as indicated by equation (6). Consequently, the controller can be developed to achieve appropriate static and dynamic performances for the MIBC.

$$C_{(S)} = k_p + k_i \frac{1}{s} \tag{6}$$

$$k_p = \frac{\cos\theta}{|G_p(j\omega_c)|} \tag{7}$$

$$k_i = \frac{-\omega_c \sin\theta}{|G_p(j\omega_c)|} \tag{8}$$

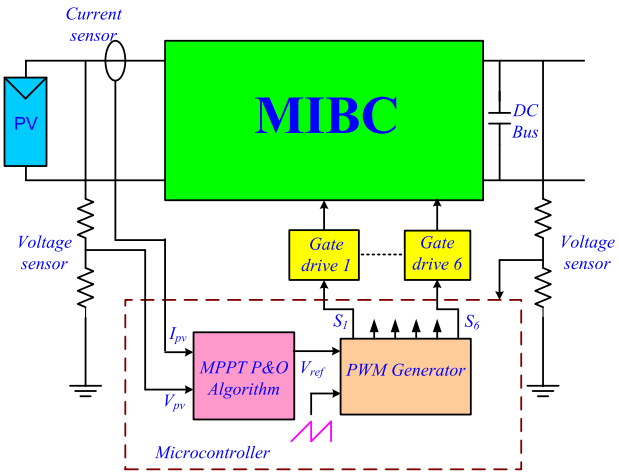

FIGURE 9. Block diagram of the MIBC with feedback control.

$$\theta = 180^{\circ} + \varphi_m - \angle G_p(j\omega_c) \tag{9}$$

where the discrete-time transfer function is Gp(s) of the open-loop system (e.g., Gv(s), or Gi(s)). Figs. 11 and 12. show the Bode plots for the proposed control loop gain based on PI control. For this work KP = 0.034, and KI = 0.0048.

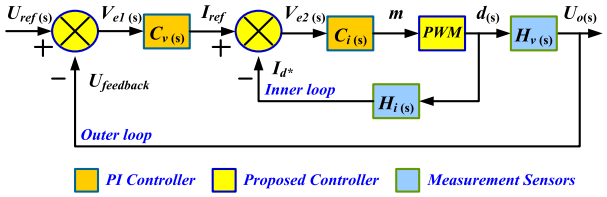

FIGURE 10. Schematic diagram of the closed-loop control strategy.

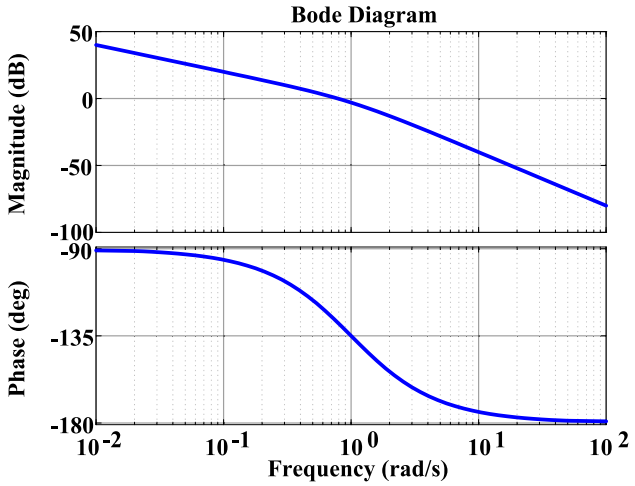

FIGURE 11. Bode diagram of voltage loop gain.

In this study, regardless of input and load voltage variations, a constant voltage of 250 V is maintained in the DC/DC converter output through the use of simple feedback PI controllers. Using a Bode diagram, PI controllers will be constructed based on the necessary phase margin PM (φm) and critical frequency (ωc).

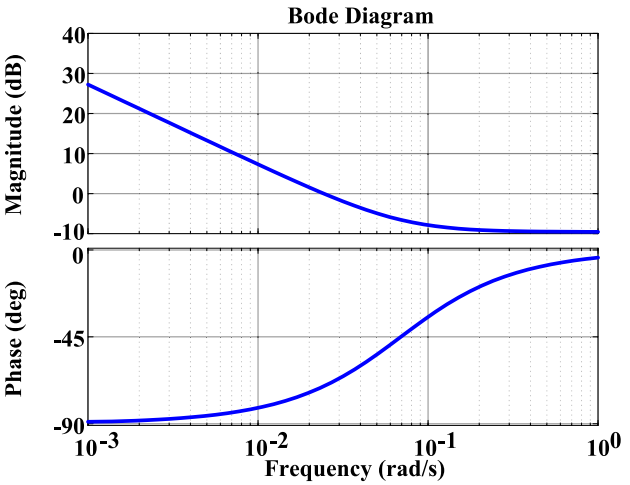

FIGURE 12. Bode diagram of current loop gain.

Where ω_c and ω_{180} are called the crossover-frequencies if $\omega_c < \omega_{180}$ is a stable system if $\omega_c = \omega_{180}$ is a marginal system if $\omega_c > \omega_{180}$ is an unstable system. It can be seen that the critical frequency (ω_c) is 0.2649 rad/sec when the phase margin (φ_m) is 36.7° (i.e. younger than ω_{180} = 0.5774 rad/sec) when the gain is 11.6 dB in Fig. 11 similarly Fig. 12. Thus the proposed converter can achieve stable operation theoretically and experimentally.

TABLE 1. Calculated parameters.

$$\because Input\ Voltage: V_i = 12V;\ Output\ Voltage: V_o = 40V \Rightarrow$$
$$\therefore D = \frac{V_o - V_i}{V_o} = \frac{40 - 12}{40} = 0.7$$
$$\because Switching\ Frequency: f_S = 100kHz \Rightarrow$$
$$\therefore T_s = \frac{1}{f_s} = \frac{1}{100 * 10^3} = 10\mu s$$
$$\because Output\ Current: I_o = 7A \Rightarrow \therefore I_{boost} = \frac{I_o}{2} = \frac{7}{2} = 3.5A$$
$$\therefore \Delta I_L = 10\% * I_{boost} = 0.1 * 3.5 \leq 0.35A$$

III. DESIGN CONSIDERATIONS FOR MIBC

A. DESIGN CONSIDERATIONS OF MAIN COMPONENTS

The Self-inductance of coupled inductors can be obtained from the current ripple expression, as shown in Table 1 as follows [53]:

$$\Delta I_L = \frac{D * V_i}{L * f_s} \Rightarrow L = \frac{D * V_i}{\Delta I_L * f_s} = 480\mu H \tag{10}$$

where ΔIL is the current ripple in the coupled inductors, and fS is the SF. The OVR is given by the expression:

$$\Delta V_o = \frac{D * V_i}{(1 - k) * R_o * C_o * f_s} \tag{11}$$

The value of capacitance is decided by the equation:

$$C_o = \frac{D * T_{swit} * V_o}{R_o * \Delta V_o} = 360\mu F \tag{12}$$

where Ts is the period time, Ro is the output resistance, and ΔVo < 50 mV is the OVR

B. DESIGNS FOR ZCS RESONANT CIRCUIT

The equivalent output impedance can be determined from the V_o and I_o given as:

$$R_o = \frac{V_o}{I_o} = \frac{30}{3} = 10\Omega \tag{13}$$

The characteristic impedance is computed as given:

$$R_o = 10\Omega \; and \; Q = 1 \; into \; \Rightarrow Z_o = \frac{R_o}{Q} = \frac{10}{1} = 10\Omega \tag{14}$$

The resonant frequency is calculated from switching frequency f_s and normalized switching frequency $f_{ns} = 0.6$ was set based on the normalized voltage gain [51]:

$$f_r = \frac{f_s}{f_{ns}} = \frac{100}{0.6} = 166.7kHz \tag{15}$$

The RI L_r is given by:

$$L_r = \frac{Z_o}{\omega} = \frac{Z_o}{2\pi f_r} = \frac{10}{2\pi * 166.7 * 10^3} = 9.6\mu H \tag{16}$$

The RC C_r is given by:

$$C_r = \frac{1}{\omega Z_o} = \frac{1}{2\pi * 166.7 * 10^3 * 10} = 95.5nF \tag{17}$$

C. SELECTION OF THE MAIN SWITCHES

MOSFETs are N-type transistors. When selecting switching devices for Q1 and Q2 MOSFETs, we must make sure that the MOSFETs can handle the switching frequency of 100 kHz. MOSFETs must also be able to handle a peak current of 7A, to meet the 90% efficiency specification [54]. For this design, we can choose suitable integrated circuits such as (MOSFETs IRF540) which give sufficient safe margins for 50V source-drain breakdown voltage.

IV. LOSSES IN THE PROPOSED MIBC

The estimated losses in the suggested converter are the losses brought on by the passive components (capacitors and inductors) and semiconductor switches (MOSFETs and DIODEs). The objective of this interpretation is just to provide an idea of the estimated losses. This research computes the efficiency using this estimate [55]. The converter's efficiency is calculated as follows:

$$\eta = \frac{P_{input\_power} - \sum_{Losses}}{P_{input\_power}} \tag{18}$$

A. INDUCTORS LOSSES

In coupled inductors, there are copper losses. Eddy currents, hysterical occurrences, and other changing magnetic field-related processes are responsible for the losses. A small amount of the energy may manifest as noise, but the majority of it is dissipated as heat. Conduction or copper losses in inductors are calculated as follows [51], [56]:

$$P_L = 2 * (I_{L\_rms})^2 * R_L \tag{19}$$

where I_{L_rms} denotes the inductor's RMS current value and R_L denotes its resistance.

B. CAPACITOR LOSSES

The equivalent capacitor resistance, which is often included in datasheets, is used to determine capacitor losses. The following formula is used to calculate capacitor losses as follows [56]:

$$P_C = (I_{C\_rms})^2 * R_C \tag{20}$$

where I_{C_rms} represents the capacitor's RMS current value and R_C represents the equivalent capacitor resistance.

C. MOSFETs (Q1 AND Q2) LOSSES

The following equations provide the MOSFET conduction losses [56], [57]:

$$P_{cond} = 2 * (I_{q\_rms})^2 * R_{ds-on} \tag{21}$$

The MOSFET switching losses are given by:

$$P_{swit} = 2 * 0.5 * I_{in} * V_o * T_{swit} * f_s \tag{22}$$

The MOSFET gate drive losses are given by:

$$P_{gate} = 2 * Q_{swit} * V_g * f_s \tag{23}$$

where R_{ds-on} is the on-resistance and Q_{sw} is the total gate drive. The MOSFET characteristics (R_{ds-on} and Q_{sw}) are given in the datasheet of the MOSFET.

D. DIODES (DQs AND Do) LOSSES

The following equation provides the diode conduction losses [58]:

$$P_D = 2 * V_f * I_{in} * (1 - K) \tag{24}$$

V. ASSESSMENT OF EFFICIENCY AND CONVERTER LOSSES

The suggested interleaved boost converter's efficiency and switching losses are computed by writing code to a MATLAB file [59]. The RMS currents in the different parts of the suggested converter in Figure 4 must be calculated as the first step in evaluating switching losses. These formulae all make the assumption of CCM for simplicity's sake, which was accurate in our investigation for around 10% of the proposed converter estimated current. For instance, in the proposed MIBC, the output current Io and inductor ripple current IL are employed to determine the RMS inductor current in Eq. (26).

RMS current of the output capacitor IC_rms, calculated in Eq. (27). Given the pertinent DC and (1–D) for the proposed MIBC, it is possible to compute the RMS switches current IQ_rms in Eq. (28) and the RMS diode's current ID_rms in Eq. (29). Figure 13 displays the MIBC losses against the HSIBC losses. Figure 14 illustrates the MIBC theoretically estimated efficiency against the HSIBC [60], [61].

$$\Delta I_L = \frac{D * V_i}{L * f_s} \tag{25}$$

$$I_{L\_rms} = \sqrt{I_o^2 + \frac{\Delta I_L^2}{12}} \tag{26}$$

$$I_{C\_rms} = I_o * \sqrt{\frac{D}{1-D}} \tag{27}$$

$$I_{Q\_rms} = \sqrt{D * I_i^2 + \frac{\Delta I_L^2}{12}} \tag{28}$$

$$I_{D\_rms} = \sqrt{(1-D) * I_i^2 + \frac{\Delta I_L^2}{12}} \tag{29}$$

Figures 13 - 14, respectively, display the outcomes of the energy losses study and the suggested converter estimated efficiency. The suggested soft-switching MIBC has 98% efficiency at 12V input voltage and 300W input power. The total MIBC losses are about 7.55W if a switching frequency of up to 100 kHz is used in the suggested MIBC design, compared to 92% for a traditional hard-switching IBC [62]. Based on that, it is clear from the calculated results that the suggested converter circuit achieves better efficiency with an improvement of 6% compared to the hard-switching converter.

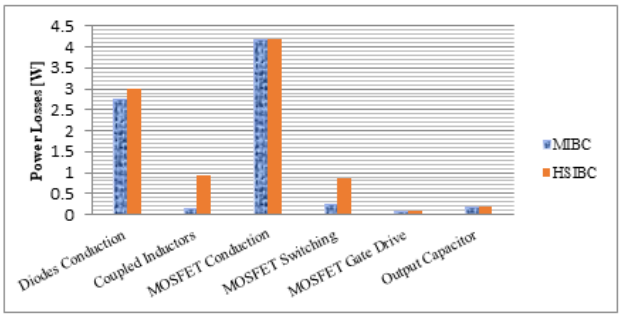

FIGURE 13. MIBC losses vs. HSIBC losses.

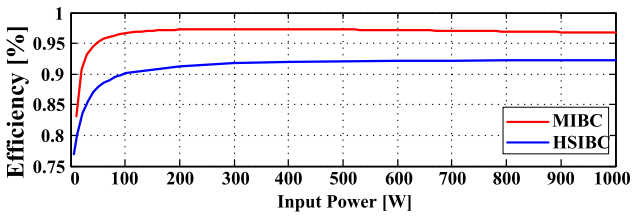

FIGURE 14. MIBC Efficiency vs. input power compared to HSIBC.

VI. RESULTS AND DISCUSSION

A. SIMULATION RESULTS

A prototype simulation was run on MATLAB SIMULINK to investigate the recommended converter's power management and soft-switching bands of the suggested converter. Table 2 below contains the recommended converter circuit settings. Figure 15 depicts the suggested MIBC simulation model. Figure 16 displays the solar radiation, voltage, current, and output power of the PV arrays. Figure 17 displays the voltage and current output of the suggested open loop MIBC circuit at $D = 0.6$. The feedback control signal V_m is formed when the feedback control system depicted in Figure 9 is used to obtain the gating signals (Q_1 and Q_2). Table 3 below shows the superiority of the suggested topology which eliminates ripples in the voltage and current output.

TABLE 2. Simulation parameters.

Items	Symbols	Values
Output Power	P_o	285W
Input Voltage	V_{in}	12V
Output Voltage	V_{out}	40V
Load Resistance	R_o	5.6Ω
Filter Capacitor	C_o	360μF
Resonant Inductors	L_{r1}, L_{r2}	9.6μH
Resonant Capacitors	C_{r1}, C_{r2}	95.5nF
Self-Inductance of CI Branch 1	L_{11}	480μH
Mutual Inductance through Branches 1 and 2	L_{12}	250μH
Self-Inductance of CI Branch 2	L_{22}	480μH
Coupled Coefficient	k	0.84
Inductor Turns No.	$T_{no.}$	25
Utilized Core	Ferrite Core	(UU-95)
Gain Parameters of PI Controller	K_P, K_I	0.034, 0.0048
Switching Frequency	F_s	100kHz
Resonant Frequency	F_r	166.7kHz

The P_{PV} and I_{PV} vary nearly linearly together with the solar radiation, as shown in Figure 16. Figure 16 displays that the PV voltage is independent of the solar radiation level as there is a complete separation between the input and output of the MIBC. Figure 17 displays the output voltage of the MIBC is almost constant, even though the system operates under MPPT control. This detects the robustness and efficacy of the suggested MIBC.

TABLE 3. Comparison between the two topologies.

Items	Output Voltage Ripple	Output Current Ripple
Hard-Switching With Feedback Control	900 mV	500 mA
Soft-Switching With Feedback Control	40 mV	30 mA

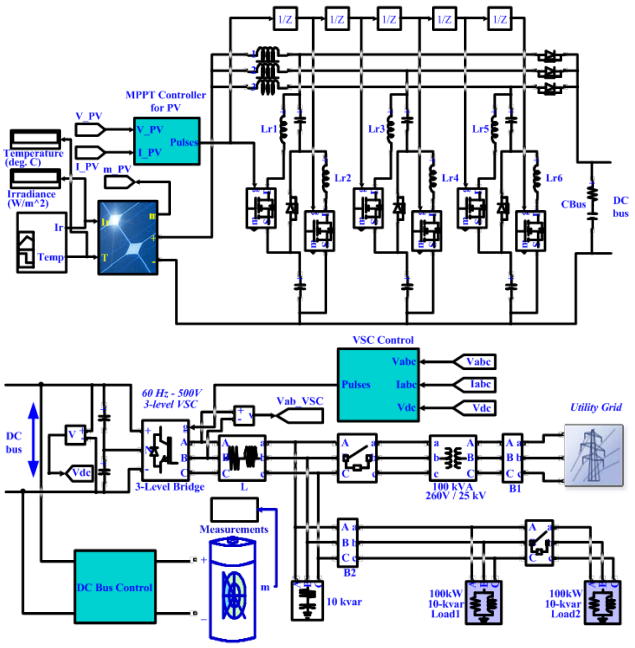

FIGURE 15. Simulation model of the suggested MIBC.

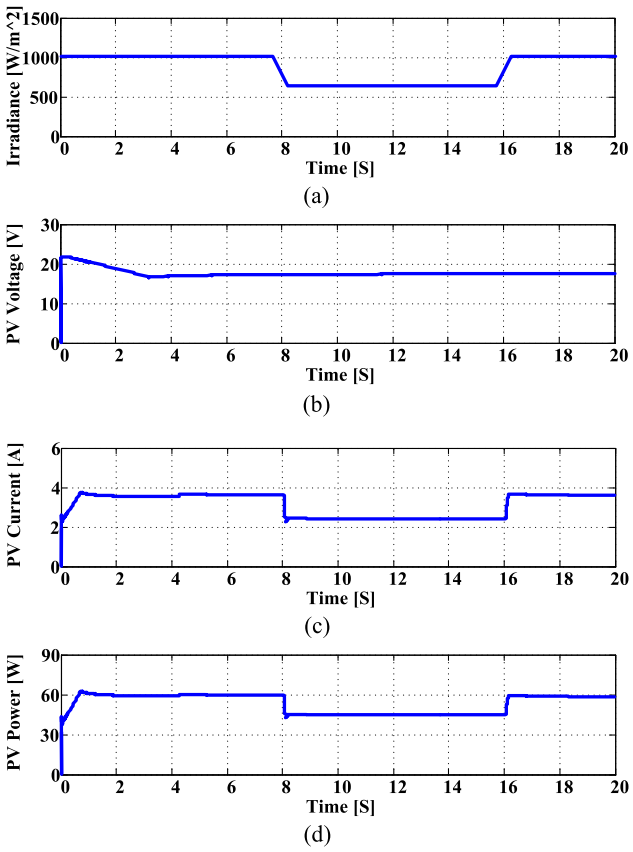

FIGURE 16. PV power flow at constant temperatures and variable radiation levels. (a) PV solar radiation curve, (b) PV voltage curve, (c) PV current curve, and (d) PV power curve.

Figure 18 shows the characteristics of DC input power regulation compared to those of the proposed symmetric

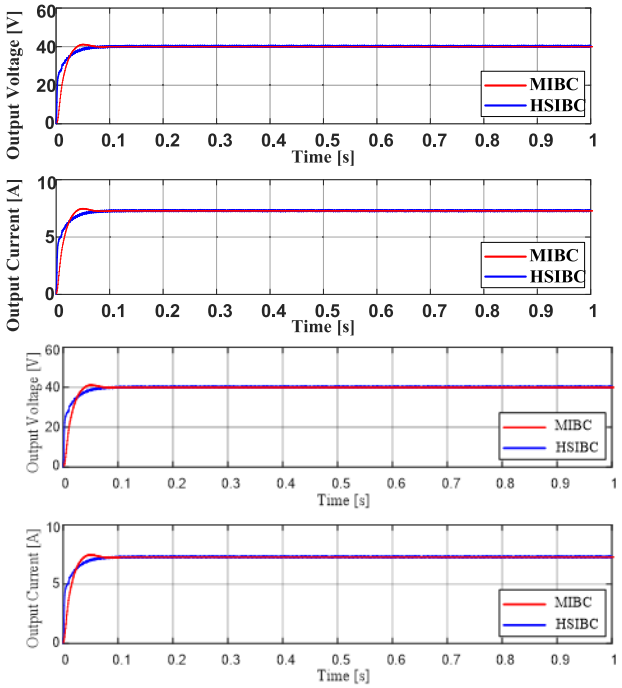

FIGURE 17. Shows the voltage and current output of the suggested MIBC, respectively at $D = 0.6$.

MIBC with an auxiliary resonant cell. The suggested MIBC can organize the input power by controlling the phase shift of the PWM from 2 kW to 0.1 kW, and 2 kW to 1 kW respectively under the SS method [63], [64]. Figure 18 illustrates the input power regulation characteristics of the suggested converter, the duty cycle SS area starts at $D = 0.40$ to $D = 0.95$, after this value ($D = 0.95$) the output voltage and power suddenly drop to a very low value. The output power of the suggested MIBC can be adjusted constantly according to the duty cycle D as a control variable, as shown in Figure 18.

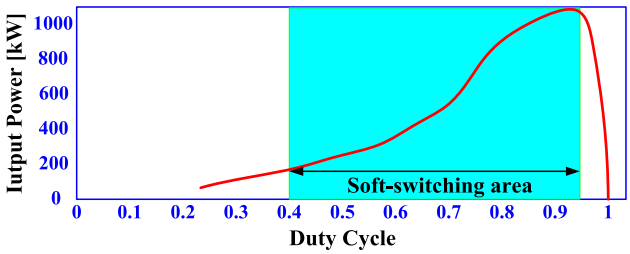

FIGURE 18. Represents duty cycle characteristics relative to input power regulation.

B. EXPERIMENTAL RESULTS

An experiential setup is performed to employ a PV array where the PV arrangement consists of 60W PV arrays, while their specifications are listed in Table 4. Figure 19 illustrates the experimental setup of the suggested converter. Figure 20 Gate control signal wave. Figure 21 (a) and (b) illustrate

experimental voltage and current waves of the switches (Q_1, Q_2), respectively. From these figures, it can be seen that the switches (Q_1, Q_2) have the properties of ZCS and ZVS during switch on and switch off. The current experimental wave of the output capacitor is shown in Figure 22. Finally, from these figures, the experiential results were validated and were largely identical to simulation results using a PIC microcontroller.

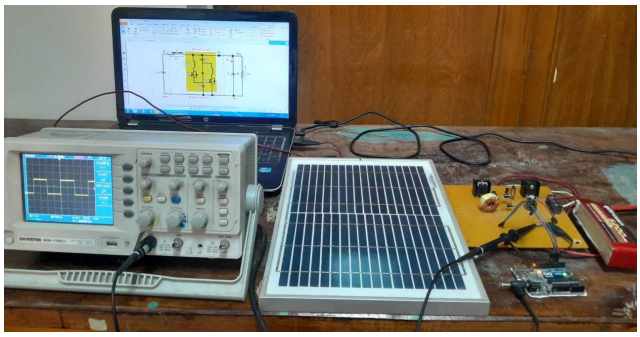

FIGURE 19. Experimental setup for MIBC.

TABLE 4. PV module parameters of the 60 W PV array at 25 ° and 1000 W/m^2.

Solar Panel Parameters	Symbols	Values
Max. Peak Power	P_m	*60W*
Max. Power Voltage	V_{mp}	*17.2V*
Max. Power Current	I_{mp}	*3.5A*
Open Circuit Voltage	V_{oc}	*21.5V*
Short Circuit Current	I_{sc}	*3.85A*

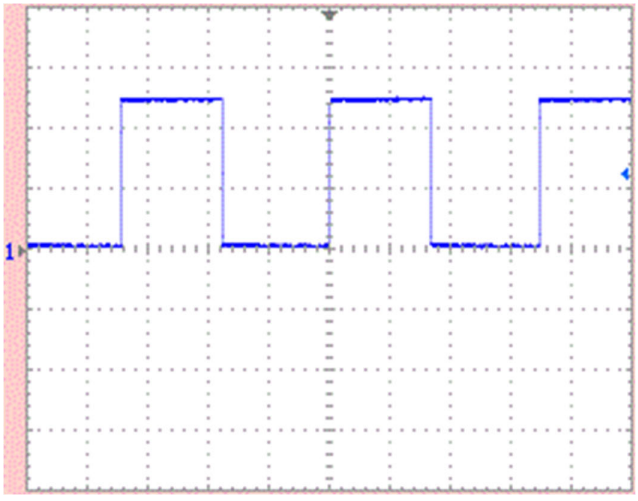

FIGURE 20. Gate control signal waveform for switches.

Semi-transparent papers were used to partially cover the PV array to replicate and create a partial shading state, which was used to evaluate the P&O MPPT algorithm's validity under various radiation conditions. The PV voltage drop due to partial shading condition appears as shown in Figure 23(a). The PV array's semi-transparent papers were then taken out to

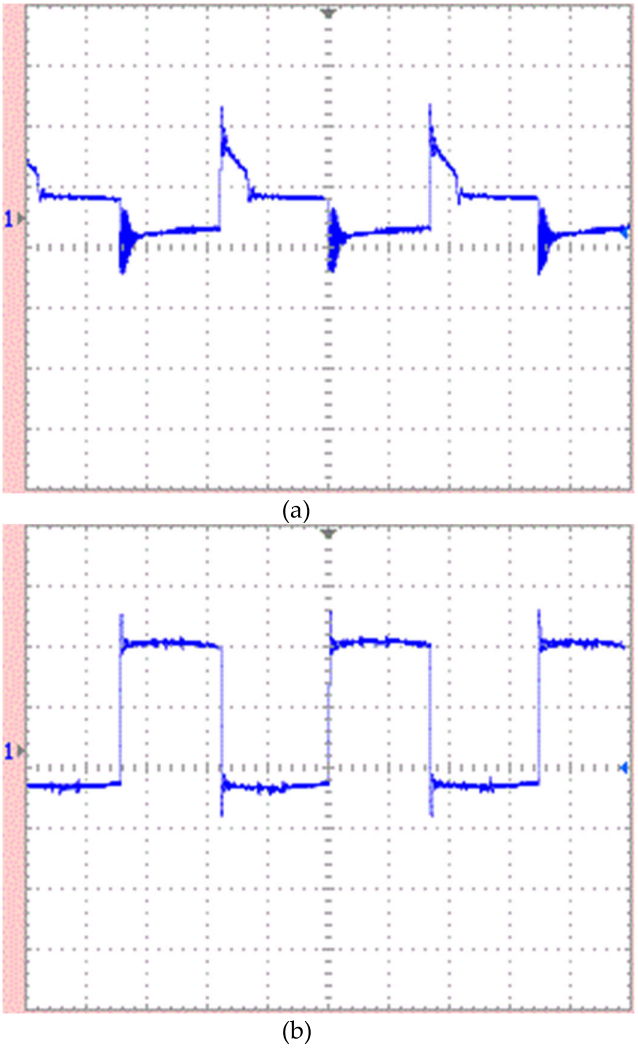

FIGURE 21. (a) & (b) Operating switches voltage and current waves.

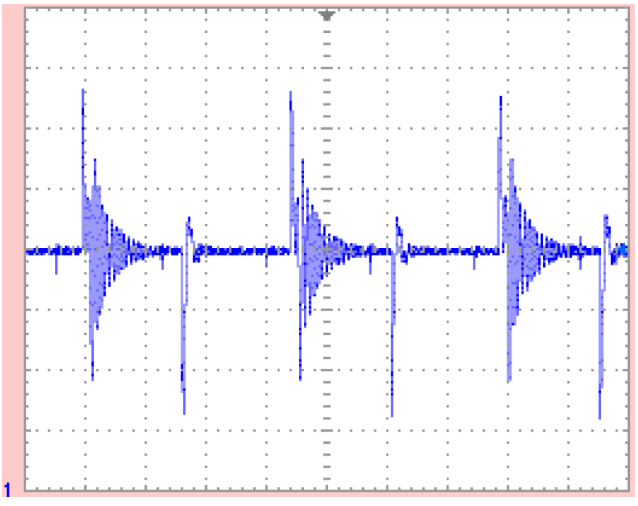

FIGURE 22. The current wave of the output capacitor.

revalidate the P&O MPPT algorithm. As seen in Figure 23(b), it appears that the PV voltage is rising once more.

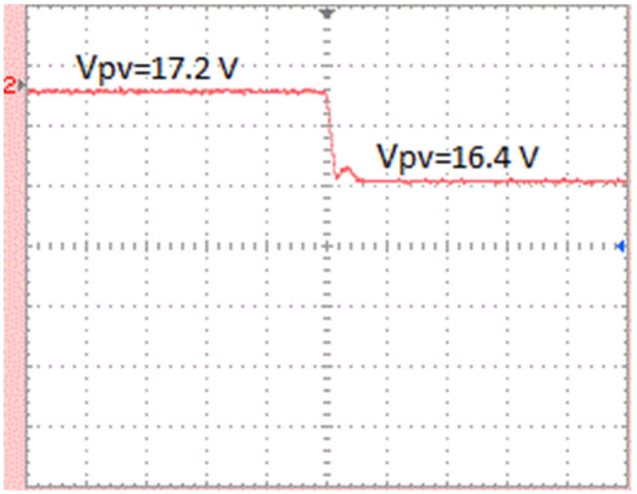

(a)

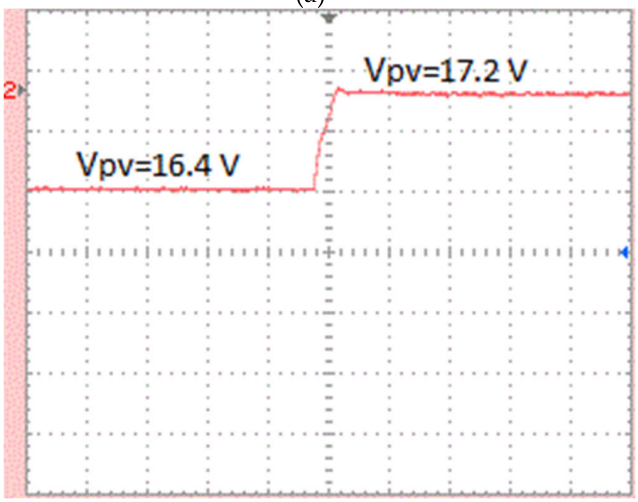

(b)

FIGURE 23. (a) & (b) PV voltage when solar radiation changes.

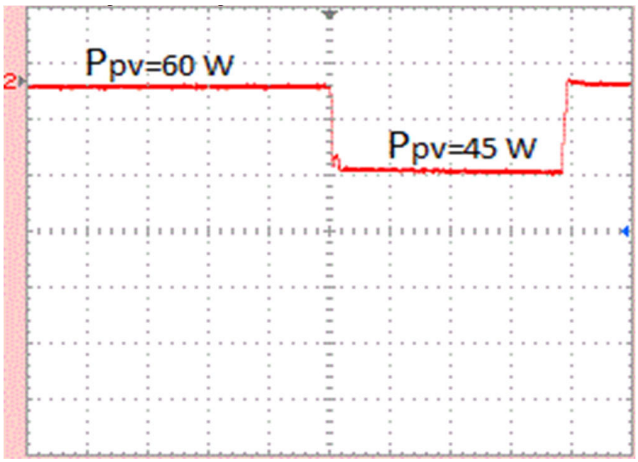

FIGURE 24. PV power when solar radiation changes.

Figure 24 displays the power extracted from the PV array utilizing the MPPT algorithm when the PV system is exposed to the same operating conditions. The results of Figures 23-24 show that the MPPT algorithm has less steady-state oscillations and reaches steady-state in a shorter time. In addition, the suggested layout guarantees optimum power production from the actual PV system by enabling optimal power generation regardless of the shading or radiation conditions of the PV system.

A comparison of the suggested MIBC and various topologies for PV modules is presented in Table 5. Given that, each converter has a various power rating, as indicated in Table 5. The efficiency is compared in terms of normalized output as a percentage of the rated output power for each converter. It should be noted that the proposed structure has the characteristic of a wide operating range and higher efficiency among other converters.

TABLE 5. Comparison between the proposed MIBC with other existing topologies.

Ref. No.	Input Voltage	Output Voltage	Voltage Gain	No. of Modes	Switching Frequency	Rated Power	Efficiency
Proposed	12*V*	40*V*	3.33	4	100*kHz*	285*W*	98%
Ref. [38] (2010)	90-256*V*	400*V*	1-3	4	100*kHz*	250*W*	95%
Ref. [39] (2011)	200*V*	400*V*	2	8	80*khz*	750*W*	95%
Ref. [40] (2011)	200*V*	400*V*	2	8	30*kHz*	1200 *W*	97.8%
Ref. [41] (2012)	200*V*	400*V*	2	9	30*kHz*	1000 *W*	96.15 %
Ref. [42] (2012)	100-200*V*	300*V*	1.5-3	4	100*kHz*	1000 *W*	97%
Ref. [43] (2012)	23*V*	30*V*	1.5	4	100*kHz*	10-60*W*	92-94%
Ref. [44] (2015)	150-230*V*	380*V*	2.53	4	30*kHz*	700*W*	96%
Ref. [45] (2017)	25*V*	50*V*	2	4	24*kHz*	100*W*	92.5%
Ref. [46] (2017)	50*V*	100*V*	2	7	100*kHz*	200*W*	95.8%
Ref. [47] (2017)	20*V*	60*V*	**3**	7	50*kHz*	250*W*	93.5%
Ref. [48] (2018)	400*V*	800*V*	2	5	20*kHz*	10000 *W*	97.5%
Ref. [49] (2020)	30*V*	100*V*	3	5	40*kHz*	500*W*	97%
Ref. [50] (2021)	48*V*	96*V*	2	7	100*kHz*	220*W*	97.6%

VII. CONCLUSION

In this study, an MIBC is presented for usage in the quick and effective charging of Li-ion batteries for renewable

energy applications integration. The suggested converter working principles and steady-state analysis are explained. Additionally, the suggested MIBC is examined, designing considerations are presented, and its many Intervals of operation are explained. This converter uses ARC to provide ZCS turn on and off for the converter main switches, thus reducing switching losses. The suggested converter outperforms the traditional hard-switching converter in terms of efficiency. These results in less ICR and lower voltage stress on the MS compared to a traditional boost converter, which lowers conduction losses. The suggested converter has a total efficiency of 98%, based on modeling and experimental data. Additionally, the suggested converter is controlled by the MPPT algorithm. The MIBC can adjust the input and output power by controlling the phase shift of the PWM method. The utilization of the CIs reduces the number of magnetic cores and other magnetic materials employed in the suggested MIBC. The OCR is decreased by increasing the coupling coefficient, which also lowers the inductor's core losses. The other feature of utilizing CIs is that the size and cost of the converter are reduced. Finally, MATLAB simulation and empirical findings demonstrated the effectiveness of the suggested converter.

The MIBC interface is used in RES applications to combine power from diverse energy sources into a unified system. Here is a summary of its advantages and disadvantages:

ADVANTAGES

1. Flexibility: An MIBC can handle power from diverse RESs (e.g., solar panels, fuel cells, wind turbines, batteries, and supercapacitors) simultaneously, allowing for a more flexible and adaptable power system.
2. Efficiency: By combining diverse RESs, these converters can optimize energy utilization and improve overall system efficiency.
3. Improved reliability: Multiple sources mean that if one source fails or becomes less productive (e.g., low sunlight for solar panels), other sources (e.g., wind power, fuel cell power, or stored battery&supercapacitor power) can compensate, resulting in a more reliable power supply.
4. Load management: A system can balance load more effectively by drawing from the most efficient source available at any given time.
5. Peak shaving: MIBC can help manage peak loads by drawing power from diverse RESs, reducing the need for additional infrastructure.
6. Storage integration: They can effectively manage the integration of energy storage systems, smoothing supply and demand.
7. Reduced need for multiple converters: Instead of needing separate converters for each power source, MIBC unified functions, reducing hardware costs and space requirements.

DISADVANTAGES

1. Design complexity: MIBCs are more complex to design and implement than single-phase converters. They require sophisticated control systems and algorithms to manage diverse power sources effectively.
2. Maintenance: The increased complexity may lead to more challenges in maintenance and troubleshooting.
3. Initial cost: Multiphase converters may have a higher initial cost due to their advanced design and capabilities, which may not be cost-effective for all applications.
4. Synchronization: Coordinating and synchronizing power from diverse RESs can be difficult, especially if the sources have various electrical characteristics.
5. System scalability: Expanding the system to add more phases or integrate additional sources can be complex and expensive, requiring careful redesign and calibration.

Overall, the MIBC provides RESs with a great deal of flexibility, dependability, and efficiency; they come to have additional complexity and possible cost concerns.

Future work will be to integrate different RES (e.g. fuel cells, wind turbines, batteries, and supercapacitors) into grid-connected PV systems to evaluate the method performance with different RES, as well as to test other parameters to improve the dynamic performance of the proposed method.

REFERENCES

[1] N. F. Ibrahim, S. A. E. M. Ardjoun, M. Alharbi, A. Alkuhayli, M. Abuagreb, U. Khaled, and M. M. Mahmoud, "Multiport converter utility interface with a high-frequency link for interfacing clean energy sources (PV Cell) and battery to the power system: Application of the HHA algorithm," *Sustainability*, vol. 15, no. 18, p. 13716, Sep. 2023, doi: 10.3390/su151813716.

[2] M. Metwally Mahmoud, "Improved current control loops in wind side converter with the support of wild horse optimizer for enhancing the dynamic performance of PMSG-based wind generation system," *Int. J. Model. Simul.*, vol. 43, no. 6, pp. 952–966, Nov. 2023, doi: 10.1080/02286203.2022.2139128.

[3] O. M. Lamine, N. Bessous, B. Abdelhalim, F. A. Banakhr, M. I. Mosaad, M. Oussama, and M. M. Mahmoud, "A combination of INC and fuzzy logic-based variable step size for enhancing MPPT of PV systems," *Int. J. Robot. Control Syst.*, vol. 4, no. 2, pp. 877–892, Jun. 2024, doi: 10.31763/ijrcs.v4i2.1428.

[4] R. Kassem, M. M. Mahmoud, N. F. Ibrahim, A. Alkuhayli, U. Khaled, A. Beroual, and H. Saleeb, "A techno-economic-environmental feasibility study of residential solar photovoltaic/biomass power generation for rural electrification: A real case study," *Sustainability*, vol. 16, no. 5, p. 2036, Feb. 2024, doi: 10.3390/su16052036.

[5] I. H. Masenge and F. Mwasilu, "Modeling and control of solar PV with battery energy storage for rural electrification," *Tanzania J. Eng. Technol.*, vol. 39, no. 1, pp. 47–58, Jun. 2020, doi: 10.52339/tjet.v39i1.518.

[6] L. Hernández-Callejo, S. Gallardo-Saavedra, and V. Alonso-Gómez, "A review of photovoltaic systems: Design, operation and maintenance," *Sol. Energy*, vol. 188, pp. 426–440, Aug. 2019, doi: 10.1016/j.solener.2019.06.017.

[7] M. ElMenshawy and A. Massoud, "Multimodule DC–DC converters for high-voltage high-power renewable energy sources," in *Proc. 2nd Int. Conf. Smart Grid Renew. Energy (SGRE)*, Nov. 2019, pp. 1–6, doi: 10.1109/SGRE46976.2019.9020690.

[8] M. Awad, A. Said, M. H. Saad, A. Farouk, M. M. Mahmoud, M. S. Alshammari, M. L. Alghaythi, S. H. E. Abdel Aleem, A. Y. Abdelaziz, and A. I. Omar, "A review of water electrolysis for green hydrogen generation considering PV/wind/hybrid/hydropower/geothermal/tidal and wave/biogas energy systems, economic analysis, and its application," *Alexandria Eng. J.*, vol. 87, pp. 213–239, Jan. 2024, doi: 10.1016/j.aej.2023.12.032.

[9] G. Masson and I. Kaizuka. (2021). *Trends in Photovoltaic Applications*. [Online]. Available: https://iea-pvps.org/wp-content/uploads/2020/02/5319-iea-pvps-report-2019-08-lr.pdf
[10] L. M. A. Bettencourt, J. E. Trancik, and J. Kaur, "Determinants of the pace of global innovation in energy technologies," *PLoS ONE*, vol. 8, no. 10, Oct. 2013, Art. no. e67864.
[11] M. F. Jalil, S. Khatoon, I. Nasiruddin, and R. C. Bansal, "Review of PV array modelling, configuration and MPPT techniques," *Int. J. Model. Simul.*, vol. 42, no. 4, pp. 533–550, Jul. 2022, doi: 10.1080/02286203.2021.1938810.
[12] N. F. Ibrahim, M. M. Mahmoud, H. Alnami, D. E. M. Wapet, S. A. E. M. Ardjoun, M. I. Mosaad, A. M. Hassan, and H. Abdelfattah, "A new adaptive MPPT technique using an improved INC algorithm supported by fuzzy self-tuning controller for a grid-linked photovoltaic system," *PLoS ONE*, vol. 18, no. 11, Nov. 2023, Art. no. e0293613, doi: 10.1371/journal.pone.0293613.
[13] A. F. Mirza, M. Mansoor, K. Zhan, and Q. Ling, "High-efficiency swarm intelligent maximum power point tracking control techniques for varying temperature and irradiance," *Energy*, vol. 228, Aug. 2021, Art. no. 120602, doi: 10.1016/j.energy.2021.120602.
[14] K. Ishaque, Z. Salam, and G. Lauss, "The performance of perturb and observe and incremental conductance maximum power point tracking method under dynamic weather conditions," *Appl. Energy*, vol. 119, pp. 228–236, Apr. 2014, doi: 10.1016/j.apenergy.2013.12.054.
[15] J.-Z. Yan, W.-H. Pan, H.-H. Wu, T. Hsu, and C.-L. Wei, "Photovoltaic energy harvesting chip with P&O maximum power point tracking circuit and novel pulse-based multiplier," *IEEE Trans. Power Electron.*, vol. 36, no. 11, pp. 12867–12876, Nov. 2021, doi: 10.1109/TPEL.2021.3082533.
[16] L. Bhukya, A. Annamraju, and S. Nandiraju, "A novel maximum power point tracking technique based on Rao-1 algorithm for solar PV system under partial shading conditions," *Int. Trans. Electr. Energy Syst.*, vol. 31, no. 9, pp. 1–23, Sep. 2021, doi: 10.1002/2050-7038.13028.
[17] S. Lyden, H. Galligan, and M. E. Haque, "A hybrid simulated annealing and perturb and observe maximum power point tracking method," *IEEE Syst. J.*, vol. 15, no. 3, pp. 4325–4333, Sep. 2021, doi: 10.1109/JSYST.2020.3021379.
[18] S. Mohanty, B. Subudhi, and P. K. Ray, "A new MPPT design using grey wolf optimization technique for photovoltaic system under partial shading conditions," *IEEE Trans. Sustain. Energy*, vol. 7, no. 1, pp. 181–188, Jan. 2016, doi: 10.1109/TSTE.2015.2482120.
[19] M. Abdillah, R. C. Batubara, N. I. Pertiwi, and H. Setiadi, "Design of maximum power point tracking system based on single ended primary inductor converter using fuzzy logic controller," *Int. J. Intell. Eng. Syst.*, vol. 15, no. 1, pp. 350–360, Oct. 2022, doi: 10.22266/IJIES2022.0228.32.
[20] T. Bennett, A. Zilouchian, and R. Messenger, "Photovoltaic model and converter topology considerations for MPPT purposes," *Sol. Energy*, vol. 86, no. 7, pp. 2029–2040, Jul. 2012, doi: 10.1016/j.solener.2012.04.005.
[21] S. Rostami, V. Abbasi, N. Talebi, and T. Kerekes, "Three-port DC–DC converter based on quadratic boost converter for stand-alone PV/battery systems," *IET Power Electron.*, vol. 13, no. 10, pp. 2106–2118, Aug. 2020, doi: 10.1049/iet-pel.2019.1025.
[22] S. Naresh, S. Peddapati, and M. L. Alghaythi, "A novel high quadratic gain boost converter for fuel cell electric vehicle applications," *IEEE J. Emerg. Sel. Topics Ind. Electron.*, vol. 4, no. 2, pp. 637–647, Apr. 2023, doi: 10.1109/JESTIE.2023.3248449.
[23] M. Schuck and R. C. N. Pilawa-Podgurski, "Ripple minimization in asymmetric multiphase interleaved DC–DC switching converters," in *Proc. IEEE Energy Convers. Congr. Expo.*, Sep. 2013, pp. 133–139, doi: 10.1109/ECCE.2013.6646691.
[24] M. Quamruzzaman, N. Mohammad, M. A. Matin, and M. R. Alam, "Highly efficient maximum power point tracking using DC–DC coupled inductor single-ended primary inductance converter for photovoltaic power systems," *Int. J. Sustain. Energy*, vol. 35, no. 9, pp. 914–932, Oct. 2016, doi: 10.1080/14786451.2014.961922.
[25] I. Alhamrouni, W. Wahab, M. Salem, N. H. A. Rahman, and L. Awalin, "Modeling of micro-grid with the consideration of total harmonic distortion analysis," *Indonesian J. Electr. Eng. Comput. Sci.*, vol. 15, no. 2, p. 581, Aug. 2019, doi: 10.11591/ijeecs.v15.i2.pp581-592.
[26] A. Al-Othman, M. Tawalbeh, R. Martis, S. Dhou, M. Orhan, M. Qasim, and A. Ghani Olabi, "Artificial intelligence and numerical models in hybrid renewable energy systems with fuel cells: Advances and prospects," *Energy Convers. Manage.*, vol. 253, Feb. 2022, Art. no. 115154, doi: 10.1016/j.enconman.2021.115154.
[27] A. Alzahrani, "Interleaved switched-inductor boost converter for photovoltaic energy application," *Arabian J. Sci. Eng.*, vol. 48, no. 5, pp. 6419–6430, May 2023, doi: 10.1007/S13369-022-07392-2.
[28] R. Aravind, B. Chokkalingam, R. Verma, S. Aruchamy, and L. Mihet-Popa, "Multi-port non-isolated DC–DC converters and their control techniques for the applications of renewable energy," *IEEE Access*, vol. 12, pp. 88458–88491, 2024, doi: 10.1109/ACCESS.2024.3413354.
[29] M. Ashraf, Y. Nazih, F. Alsokhiry, K. H. Ahmed, A. S. Abdel-Khalik, and Y. Al-Turki, "A new hybrid dual active bridge modular multilevel based DC–DC converter for HVDC networks," *IEEE Access*, vol. 9, pp. 62055–62073, 2021, doi: 10.1109/ACCESS.2021.3074543.
[30] S. Mateen, M. Amir, A. Haque, and F. I. Bakhsh, "Ultra-fast charging of electric vehicles: A review of power electronics converter, grid stability and optimal battery consideration in multi-energy systems," *Sustain. Energy, Grids Netw.*, vol. 35, Sep. 2023, Art. no. 101112, doi: 10.1016/j.segan.2023.101112.
[31] K. F. Sayed, M. Nakaoka, K. Morimoto, and S. K. Kwon, "New high-frequency linked half-bridge soft-switching PWM DC–DC converter with input DC rail side active edge resonant snubbers," *IET Power Electron.*, vol. 3, no. 5, p. 774, 2010, doi: 10.1049/iet-pel.2009.0025.
[32] M. R. Rogina, A. Rodriguez, A. Vazquez, and D. G. Lamar, "Improving the efficiency of SiC-based synchronous boost converter under variable switching frequency TCM and different input/output voltage ratios," *IEEE Trans. Ind. Appl.*, vol. 55, no. 6, pp. 7757–7764, Nov. 2019, doi: 10.1109/TIA.2019.2939737.
[33] M. Salem, A. Jusoh, M. Dahidah, D. Ishak, A. Richelli, I. Alhamroni, and M. Kamarol, "Improved topology of three-phase series resonant DC–DC boost converter with variable frequency control," *Alexandria Eng. J.*, vol. 61, no. 2, pp. 1701–1713, Feb. 2022, doi: 10.1016/j.aej.2021.06.078.
[34] R. Venugopal, C. Balaji, A. Dominic Savio, R. Narayanamoorthi, K. M. AboRas, H. Kotb, Y. Y. Ghadi, M. Shouran, and E. Elgamli, "Review on unidirectional non-isolated high gain DC–DC converters for EV sustainable DC fast charging applications," *IEEE Access*, vol. 3, pp. 1–16, 2023, doi: 10.1109/ACCESS.2023.3276860.
[35] H. Saleeb, K. Sayed, A. Kassem, and R. Mostafa, "Control and analysis of bidirectional interleaved hybrid converter with coupled inductors for electric vehicle applications," *Electr. Eng.*, vol. 102, no. 1, pp. 195–222, Mar. 2020, doi: 10.1007/s00202-019-00860-3.
[36] R. H. Ashique, Z. Salam, M. H. Maruf, A. Shihavuddin, M. T. Islam, M. F. Rahman, P. Kotsampopoulos, and H. H. Fayek, "A comparative analysis of soft switching techniques in reducing the energy loss and improving the soft switching range in power converters," *Electronics*, vol. 11, no. 7, p. 1062, Mar. 2022, doi: 10.3390/electronics11071062.
[37] K. Sayed, E. H. E. Zohri, and H. Mahfouz, "Analysis and design for interleaved ZCS buck DC–DC converter with low switching losses," *Int. J. Power Electron.*, vol. 8, no. 3, p. 210, 2017, doi: 10.1504/ijpelec.2017.085076.
[38] Y. Shi, X.-W. Gui, J. Xi, X. Wang, and X. Yang, "Large power hybrid soft switching mode PWM full bridge DC–DC converter with minimized turn-on and turn-off switching loss," *IEEE Trans. Power Electron.*, vol. 34, no. 12, pp. 11629–11644, Dec. 2019, doi: 10.1109/TPEL.2019.2904982.
[39] R. Phukan, S. Ohn, S. Nielebock, G. Mondal, D. Dong, and R. Burgos, "Comparison between interconnected filter blocks for three-phase AC–DC interleaved converters," *IEEE J. Emerg. Sel. Topics Power Electron.*, vol. 10, no. 5, pp. 5956–5968, Oct. 2022, doi: 10.1109/JESTPE.2022.3179335.
[40] M. V. Naik and P. Samuel, "Analysis of ripple current, power losses and high efficiency of DC–DC converters for fuel cell power generating systems," *Renew. Sustain. Energy Rev.*, vol. 59, pp. 1080–1088, Jun. 2016, doi: 10.1016/j.rser.2016.01.029.
[41] B. Akin, "Comparison of conventional and interleaved PFC boost converters for fast and efficient charge of Li-Ion batteries used in electrical cars," in *Proc. Int. Conf. Power Energy Syst.*, vol. 13, 2012, pp. 499–504.
[42] P. Alavi, A. Khoshkbar-Sadigh, E. Babaei, P. Mohseni, V. Marzang, and I. Talebian, "New auxiliary circuit for boost converter to achieve soft-switching operation and zero input current ripple," *IET Power Electron.*, vol. 13, no. 17, pp. 3910–3921, Dec. 2020, doi: 10.1049/iet-pel.2020.0815.
[43] M. Pahlavandust and M. R. Yazdani, "Single-switch boost DC–DC converter with zero-current-switching, high power density and low electromagnetic interference," *Int. J. Electron. Commun.*, vol. 121, Jul. 2020, Art. no. 153229.
[44] R. H. Ashique and Z. Salam, "A family of true zero voltage zero current switching (ZVZCS) nonisolated bidirectional DC–DC converter with wide soft switching range," *IEEE Trans. Ind. Electron.*, vol. 64, no. 7, pp. 5416–5427, Jul. 2017, doi: 10.1109/TIE.2017.2669884.

[45] E. Babaei, A. Abbasnezhad, M. Sabahi, and S. H. Hosseini, "Analysis and design of a soft-switching boost DC/DC converter," *IET Power Electron.*, vol. 10, no. 11, pp. 1353–1362, Sep. 2017, doi: 10.1049/iet-pel.2016.0388.

[46] N. A. Ahmed, B. N. Alajmi, I. Abdelsalam, and M. I. Marei, "Soft switching multiphase interleaved boost converter with high voltage gain for EV applications," *IEEE Access*, vol. 10, pp. 27698–27716, 2022, doi: 10.1109/ACCESS.2022.3157050.

[47] G. Spiazzi, "Analysis and design of the soft-switched clamped-resonant interleaved boost converter," *CPSS Trans. Power Electron. Appl.*, vol. 4, no. 4, pp. 276–287, Dec. 2019, doi: 10.24295/CPSSTPEA.2019.00026.

[48] S. Habib, M. M. Khan, F. Abbas, A. Ali, M. T. Faiz, F. Ehsan, and H. Tang, "Contemporary trends in power electronics converters for charging solutions of electric vehicles," *CSEE J. Power Energy Syst.*, vol. 6, no. 4, pp. 911–929, Dec. 2020, doi: 10.17775/CSEEJPES.2019.02700.

[49] M. R. Ahmed, R. Todd, and A. J. Forsyth, "Predicting SiC MOSFET behavior under hard-switching, soft-switching, and false turn-on conditions," *IEEE Trans. Ind. Electron.*, vol. 64, no. 11, pp. 9001–9011, Nov. 2017, doi: 10.1109/TIE.2017.2721882.

[50] A. Almutairi, K. Sayed, N. Albagami, A. G. Abo-Khalil, and H. Saleeb, "Multi-port PWM DC–DC power converter for renewable energy applications," *Energies*, vol. 14, no. 12, p. 3490, Jun. 2021, doi: 10.3390/en14123490.

[51] T. Shamsi, M. Delshad, E. Adib, and M. R. Yazdani, "A new simple-structure passive lossless snubber for DC–DC boost converters," *IEEE Trans. Ind. Electron.*, vol. 68, no. 3, pp. 2207–2214, Mar. 2021, doi: 10.1109/TIE.2020.2973906.

[52] H. M. I. Saleeb, M. M. Mahmoud, N. F. Ibrahim, A. Alkuhayli, U. Khaled, A. Beroual, and R. Kassem, "Highly efficient isolated multiport bidirectional DC/DC converter for PV applications," *IEEE Access*, vol. 12, pp. 114480–114494, 2024, doi: 10.1109/ACCESS.2024.3442711.

[53] K. Sayed, M. G. Gronfula, and H. A. Ziedan, "Novel soft-switching integrated boost DC–DC converter for PV power system," *Energies*, vol. 13, no. 3, p. 749, Feb. 2020, doi: 10.3390/en13030749.

[54] K. Sayed, E. El-Zohri, F. Naguib, and H. Mahfouz, "Performance evaluations of interleaved ZCS boost DC–DC converters using quasi-resonant switch blocks for PV interface," *IOSR J. Electr. Electron. Eng. Ver. III*, vol. 10, no. 4, pp. 1676–2278, 2015.

[55] B. Vural, O. Erdinc, and M. Uzunoglu, "Parallel combination of FC and UC for vehicular power systems using a multi-input converter-based power interface," *Energy Convers. Manage.*, vol. 51, no. 12, pp. 2613–2622, Dec. 2010, doi: 10.1016/j.enconman.2010.05.027.

[56] A. Rodriguez, A. Vazquez, M. R. Rogina, and F. Briz, "Synchronous boost converter with high efficiency at light load using QSW-ZVS and SiC MOSFETs," *IEEE Trans. Ind. Electron.*, vol. 65, no. 1, pp. 386–393, Jan. 2018, doi: 10.1109/TIE.2017.2716864.

[57] P. Purna Chandra Rao, R. Anandhakumar, and L. Shanmukha Rao, "Analysis of a novel soft switching bidirectional DC–DC converter for electric vehicle," *Bull. Electr. Eng. Informat.*, vol. 12, no. 5, pp. 2665–2672, Oct. 2023, doi: 10.11591/eei.v12i5.4505.

[58] M. Esteki, M. Mohammadi, M. R. Yazdani, E. Adib, and H. Farzanehfard, "Family of soft-switching pulse-width modulation converters using coupled passive snubber," *IET Power Electron.*, vol. 10, no. 7, pp. 792–800, Jun. 2017, doi: 10.1049/iet-pel.2016.0362.

[59] K. Fathy, K. Morimoto, T. Doi, H. Lee, and M. Nakaoka, "An asymmetrical switched capacitor and lossless inductor quasi-resonant snubber-assisted ZCS-PWM DC–DC converter with high frequency link," in *Proc. 5th Int. Power Electron. Motion Control Conf.*, Aug. 2006, pp. 1–5, doi: 10.1109/IPEMC.2006.297279.

[60] S.-H. Park, G.-R. Cha, Y.-C. Jung, and C.-Y. Won, "Design and application for PV generation system using a soft-switching boost converter with SARC," *IEEE Trans. Ind. Electron.*, vol. 57, no. 2, pp. 515–522, Feb. 2010, doi: 10.1109/TIE.2009.2036025.

[61] D.-Y. Jung, Y.-H. Ji, S.-H. Park, Y.-C. Jung, and C.-Y. Won, "Interleaved soft-switching boost converter for photovoltaic power-generation system," *IEEE Trans. Power Electron.*, vol. 26, no. 4, pp. 1137–1145, Apr. 2011, doi: 10.1109/TPEL.2010.2090948.

[62] R. Kadri, J.-P. Gaubert, and G. Champenois, "Nondissipative string current diverter for solving the cascaded DC–DC converter connection problem in photovoltaic power generation system," *IEEE Trans. Power Electron.*, vol. 27, no. 3, pp. 1249–1258, Mar. 2012, doi: 10.1109/TPEL.2011.2164268.

[63] H. Saleeb, K. Sayed, A. Kassem, and R. Mostafa, "Power management strategy for battery electric vehicles," *IET Electr. Syst. Transp.*, vol. 9, no. 2, pp. 65–74, Jun. 2019, doi: 10.1049/iet-est.2018.5026.

[64] K. Sayed, A. G. Abo-Khalil, and A. S. Alghamdi, "Optimum resilient operation and control DC microgrid based electric vehicles charging station powered by renewable energy sources," *Energies*, vol. 12, no. 22, p. 4240, Nov. 2019, doi: 10.3390/en12224240.

RASHA KASSEM received the B.S. degree in electrical and the master's and Ph.D. degrees in power electronics from Sohag University, Sohag, Egypt, in 2010, 2015, and 2020, respectively. She is a Lecturer with the Electrical Department, Faculty of Technology Education, Sohag University. Her research interests include power quality, flyback converters, PWM high-frequency inverters, electric vehicles, induction motor, energy storage devices, and their applications for battery charging.

NAGWA F. IBRAHIM received the B.S. degree from the Faculty of Industrial Education, Suez Canal University, Suez, Egypt, in 2008, and the M.Sc. and Ph.D. degrees from the Faculty of Industrial Education, Suez University, Suez, in 2015 and 2019, respectively. She is currently an Assistant Professor with the Department of Electrical Power and Machine, Faculty of Technology and Education, Suez University. Her research interests include renewable energy sources, power system protection, power electronics, high voltage direct current (HVDC), control and power quality issues, and control of power electronic converters and electrical machine drives.

MOHAMED METWALLY MAHMOUD was born in Sohag, Egypt. He received the B.Sc., M.Sc., and Ph.D. degrees in electrical engineering from Aswan University, Egypt, in 2015, 2019, and 2022, respectively. He is currently a Professor (Assistant) at Aswan University. His research interests include performance improvement of wind generators, optimization methods, intelligent controllers, fault ride-through capability, power quality, FACTS tools, and energy storage systems. He is the author or co-author of many refereed journals and conference papers. He reviews for some of well-known publishers (IEEE, Springer, Wiley, Elsevier, Taylor & Francis, and Sage). He has been awarded Aswan University prizes for international publishing, in 2020, 2021, 2022, and 2023, respectively.

ABDULAZIZ ALKUHAYLI (Member, IEEE) received the B.Sc. degree in electrical engineering from King Saud University, Riyadh, Saudi Arabia, in 2006, the M.S. degree in electrical engineering from Missouri University of Science and Technology, Rolla, MO, USA, in 2013, and the Ph.D. degree in electrical engineering from North Carolina State University, Raleigh, NC, USA, in 2018. From 2006 to 2009, he was an Operation Engineer with the Energy Control Center, Saudi Electricity Company. He is currently an Assistant Professor with the Department of Electrical Engineering, King Saud University. His research interests include energy management, renewable energy systems, flexible AC transmission systems, power system stability, and smart grids.

USAMA KHALED received the B.Sc. and M.Sc. degrees in electrical engineering from Aswan University, Egypt, in 1998 and 2003, respectively, and the Ph.D. degree in electrical engineering from Cairo University, Egypt, and Kyushu University, Japan, through a Joint Scholarship, in 2010. Since 2000, he has been with the Department of Electrical Power Engineering, Faculty of Energy Engineering, Aswan University. He has been an Assistant Professor and an Associate Professor with the College of Engineering, King Saud University, since 2014 and 2018, respectively. He is currently a Professor and the Head of the Electrical Engineering Department, Faculty of Engineering, Aswan University. He is the author/co-author of more than 100 technical papers in refereed journals and conferences. His research interests include nano-dielectric materials, applied electrostatics, renewable energy, and high voltage technologies.

ABDERRAHMANE BEROUAL (Life Fellow, IEEE) was the Head of the High Voltage Group, AMPERE Laboratory, CNRS; a Scientific Expert with the Super Grid Institute; responsible of the master's research program in electrical engineering, from 2013 to 2015. He is currently a Distinguished Professor with the Ecole Centrale de Lyon, University of Lyon, France. He is also a Distinguished Visiting Professor of the U.K. Royal Academy of Engineering, Cardiff University, and King Saud University, Saudi Arabia. He has supervised more than 45 Ph.D. theses. He is the author/co-author of more than 500 technical articles, including more than 220 refereed journal articles, five patents, two books, and six book chapters. His main research interests include high-voltage insulation, outdoor insulation, dielectric materials, long air gaps discharge and lightning, modeling of discharges, and composite materials. He is a member of many advisory committees of international conferences, and a Technical Committee of IEEE CEIDP and UF10 Technical Commission–MT30 of IEC. He was a recipient of the 2016 IEEE T. Dakin Award. He has chaired the International Study Group on Streamer Propagation in Liquids of the IEEE–DEIS (1994–1998). He was an Associate Editor of IEEE TRANSACTIONS ON DIELECTRICS AND ELECTRICAL INSULATION (2018–2020).

HEDRA MAHFOUZ IBRAHIM SALEEB received the B.Sc. degree in electrical power and machines, the M.Sc. degree in power electronics, and the Ph.D. degree in electric vehicles from Sohag University, Sohag, Egypt, in 2010, 2015, and June 2020, respectively. He is currently a Lecturer with the Department of Electrical Engineering, Faculty of Technology and Education, Sohag University. His research interests include artificial intelligence, electric vehicles, power quality, soft-switched power converters, energy storage devices, and their applications to the power systems.